EPJ Web of Conferences **349**, 01007 (2026) https://doi.org/10.1051/epjconf/202634901007
EMAS 2025

Water content and iron oxidation state analysis of silicate glass using the electron probe

Ery Hughes[1,2*], *Ben* Buse[3], *Stuart* Kearns[3], *Geoff* Kilgour[1], and *Jon* Blundy[4]

[1]Volcanology Team, The New Zealand Institute for Earth Science Limited, Aotearoa New Zealand
[2]Department of Earth Sciences, University College London, UK
[3]School of Earth Sciences, University of Bristol, UK
[4]Department of Earth Sciences, University of Oxford, UK

Abstract. The water content (H_2O) and iron oxidation state (Fe^{3+}/Fe_T) of silicate glass are useful compositional parameters to measure in volcanology and igneous petrology due to: (1) their influence on the chemical and physical properties of magmas, and (2) their use in constraining the pressure-temperature-composition conditions of magma storage and ascent. We present techniques using electron probe microanalysis (EPMA) that carefully mitigate for the effects of sub-surface charging, which causes beam damage and modifies X-ray emission. The calibrated volatiles-by-difference technique quantifies H_2O (assuming that this is the dominant volatile species) in silicate glass at a spatial resolution of 5–10 μm diameter with uncertainties of ±0.5–0.7 wt% and has been tested on basaltic glasses. The time-dependent-ratio flank method quantifies Fe^{3+}/Fe_T at a spatial resolution of 20–60 μm diameter with uncertainties of ±0.1 and has been tested on a wide range of basaltic and peralkaline rhyolitic glasses. EPMA often requires straightforward sample preparation and is more accessible than other techniques used to quantify both H_2O and Fe^{3+}/Fe_T (e.g., SIMS, FTIR, Raman, XANES, Mössbauer), although uncertainties are typically larger using EPMA. For H_2O, the spatial resolution of EPMA is often higher than other techniques (e.g., SIMS, FTIR), whereas for Fe^{3+}/Fe_T it is often lower (e.g., Raman, XANES). Both EPMA techniques can be used on natural (e.g., melt inclusion and matrix glass) and experimental glasses, in addition to standard EPMA for quantification of major and minor element concentrations, for extensive chemical characterisation using EPMA.

1 Introduction

Magmas are multiphase mixtures of melt, crystals, and vapour bubbles. During ascent, decreasing pressure causes volatiles (e.g., H_2O, CO_2, S, Cl, etc.) dissolved in the melt to exsolve into a vapour phase creating bubbles that increase the buoyancy of the magma, driving it to the surface [e.g., 1]. This also changes the chemistry of the melt during ascent, causing the volatile content to decrease and variations in Fe^{3+}/Fe_T (Fig. 1A). The chemistry of the melt phase, including the volatile content (especially H_2O) and Fe^{3+}/Fe_T, are important

* Corresponding author: ery.hughes@ucl.ac.uk

in controlling the chemical and physical properties of the magma (e.g., phase equilibria, melt density and viscosity, vapour speciation, etc. [e.g., 2-6]) and are therefore important to quantify in volcanology and igneous petrology.

Changes in the chemistry of the melt can be assessed by analysing melt inclusions: tiny pockets of melt that are trapped inside crystals as they grow in the magma, providing a sample of the melt at the time of entrapment (Fig. 1B, [7]). These melt inclusions and any melt surrounding the crystals quench to a glass upon eruption, with the latter termed matrix glass (Fig. 1B). Sometimes melt inclusions and matrix glasses are not completely glassy and contain crystals (e.g., microlites) and/or bubbles, which can complicate analysis and interpretation (see [7] for information on these issues for melt inclusions). Melt inclusions are typically small (10s to rarely 100s of µm across) and are therefore normally analysed using a variety of microanalytical techniques to capture their full chemistry [7]. Here we provide an overview of two electron probe techniques to measure the water content (H_2O) [8] and iron oxidation state (Fe^{3+}/Fe_T) [9] of silicate glass, developed to be applied to melt inclusions but that can also be used on matrix and experimental glasses.

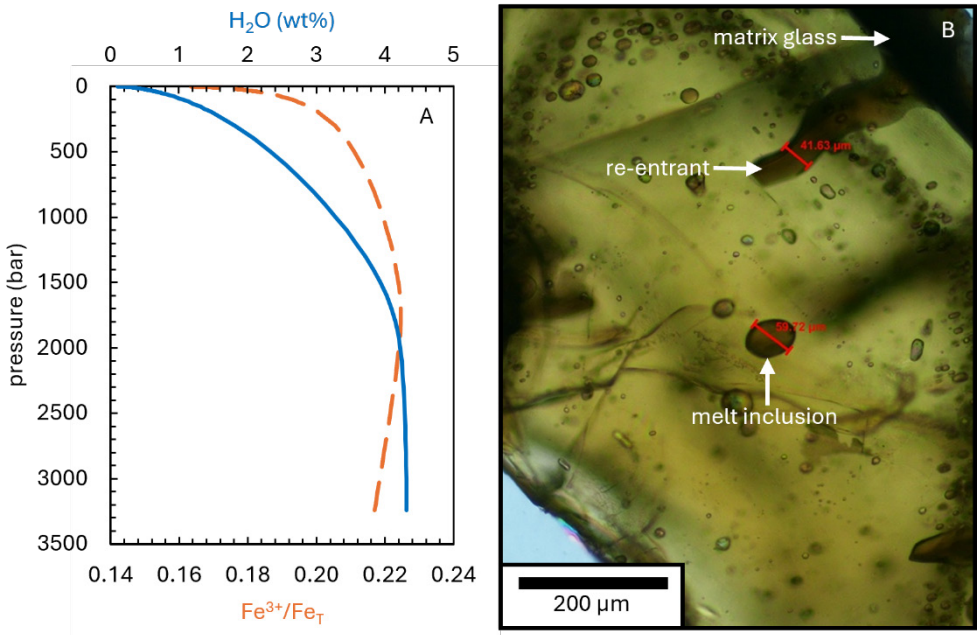

Fig. 1. (A) Example of how water content of the melt (H_2O: solid curve, upper x-axis) and iron oxidation state (Fe^{3+}/Fe_T: dashed curve, lower x-axis) vary with decreasing pressure during magma ascent (model results from [10]). **(B)** Transmitted light photomicroscope image of an olivine crystal from basaltic scoria (Stromboli, Italy) containing several melt inclusions (one is labelled in the centre as an example), a re-entrant (sometimes called an embayment), and matrix glass around the edge (labelled in the upper-right corner).

2 Water content using calibrated volatiles-by-difference

The electron probe cannot directly measure the water content of silicate glass (or any material) but can be used to indirectly quantify the water content using the "Volatiles-By-Difference" (VBD) technique [8, 11-15]. This requires measuring all the major and minor elements in the silicate glass, converting them to oxides, and assuming the remaining mass of the sample is water. This is justified as magmatic volatiles are typically dominated by H_2O.

As a by-difference technique, care must be taken to accurately and precisely quantify the elements that can be measured as the uncertainty on the water content is the quadratic sum of all the measured elements uncertainties' (typically ±0.5–0.7 wt%; [8]).

An example EPMA set-up is shown in Table 1, but there are several considerations to achieve accurate and precise VBD analyses. The unmeasured mass of the sample includes all unmeasured elements (e.g., trace elements, CO_2, etc.), so if these are in high concentration assuming VBD is only water will overestimate the true water content. Also, VBD is not simply 100 wt% minus the measured analytical total. Hydrogen must be specified as an element in the matrix correction to account for the effect of H_2O on X-ray emissions (e.g., X-ray absorption due to O in H_2O), otherwise VBD can be overestimated by ~1 wt% [12, 16-18]. Additionally, the oxidation state of multivalent elements in sufficiently high concentrations (e.g., Fe, S) should be independently constrained to reduce the uncertainty when converting from elements to oxides (e.g., uncertainty in basalts due to unknown Fe^{3+}/Fe_T is up to ±0.7 wt%; [8]). Secondary standards of similar composition to the unknowns are crucial for evaluating precision and accuracy of the analyses.

Table 1. Example EPMA set-up for VBD analysis of hydrous basaltic glass from [8].

Spectrometer set-up, elements (in analytical order), and *standards*‡				
PETJ	TAP	TAPH	PETH	LIFL
Ca* *Wollastonite*	Si* *Albite*	Na* *Albite*	K* *Sanidine*	Fe* *Andradite*
Ti *TiO_2*	Al *Sanidine*	Mg *Olivine*	P *Apatite*	Mn *Mn-metal*
Cl *NaCl*			S *Barite*†	
Analytical conditions		**Other**		
Accelerating voltage: 15 kV		Peak counting time: 60 s (K is 120 s)		
Beam current: 10 nA		Backgrounds: MAN		
Beam diameter: 5–10 µm		*TDI measurements collected		

Notes: ‡Primary standards for peaking and calibration are shown in italics. †Peak position standard for S should have similar S^{6+}/S_T to unknowns as the S peak position depends on oxidation state [19].

Hydrous glasses are electrical insulators, meaning they trap electrons within the sample [20]. This creates a region of negative charge at depth that generates an electric field within the sample [20], called sub-surface charging. This has two important effects on glass EPMA. Firstly, mobile cations (e.g., Na^+, K^+) migrate towards the region of negative charge causing their concentration in the analytical volume to decrease over time [21]. Concurrently, the relative concentration of immobile elements (e.g., Si, Al) increases due to "grow-in" [21-22]. To mitigate for this: (1) use the largest beam diameter that maintains a homogeneous analytical volume (no crystals, such as microlites, bubbles can be present within the analytical volume) and spectrometer focus (i.e., <20 µm); (2) use the lowest beam current that achieves the required analytical precision in a reasonable time; (3) reduce counting times whilst achieving the required analytical precision (e.g., use Mean Atomic Number, MAN, rather than off-peak backgrounds; [18]); and (4) analyse problematic elements first (e.g., Na, K, Si), whilst collecting time dependent intensity (TDI) data so that a correction can be applied if needed [21].

Secondly, the incoming electrons are decelerated by the internal electric field reducing their energy meaning they generate fewer X-rays than if no sub-surface charging was occurring [20]. Typically, minerals are used as standards because they are more stable and well-characterised. However, the intensity of sub-surface charging at the same analytical conditions is expected to be less for minerals than for hydrous glasses because charge trapping sites are more common in amorphous materials [23]. Hence, the measured concentration of elements in hydrous glasses is underestimated, causing VBD to be overestimated, which has been shown for literature and modelled data [8]. To mitigate for

this, a set of hydrous glasses with known H_2O (and ideally CO_2 and Fe^{3+}/Fe_T) analysed using the same analytical conditions in the same session can be used to calibrate VBD for unknown glasses (Fig. 2) [8, 24]. A linear regression ($y = mx + c$) is applied to the measured VBD (x) and the independent volatile content (y) of the VBD standards, which is then used on the measured VBD of the unknown glasses. This improves the accuracy for VBD from an offset of ~1 wt% to within ±0.1 wt% [8]. The example in Figure 2 uses the St8.1 suite of hydrous, relatively oxidised (Fe^{3+}/Fe_T ~ 0.66), basaltic experimental glasses from [25]. Secondary VBD standards can be used to evaluate the accuracy and precision of the final water contents.

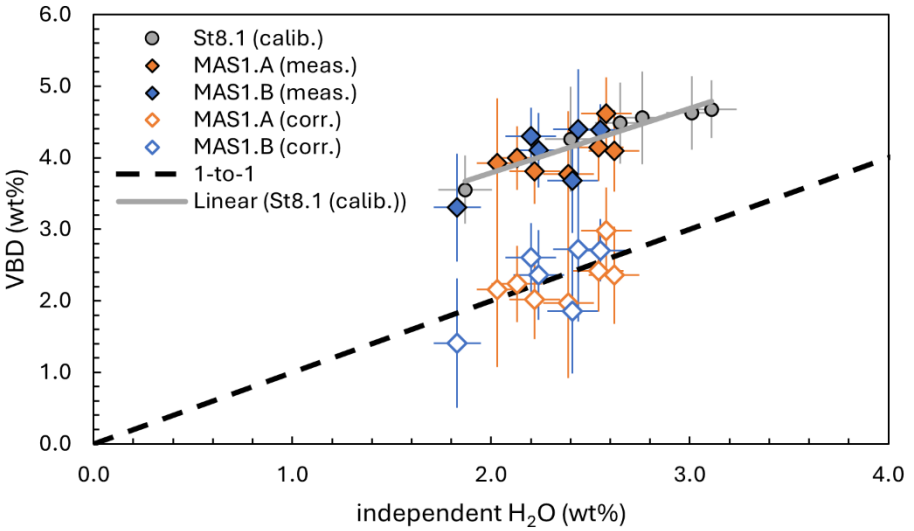

Fig. 2. Example of applying calibrated volatiles-by-difference (VBD) to experimental glasses. The VBD calibration (calib. – solid line) glasses are shown as filled circles (St8.1), which are applied to the measured (meas.) data shown as filled diamonds (MAS1.A and MAS1.B), resulting in corrected (corr.) VBD estimates shown as open diamonds similar to the independent H_2O using SIMS and FTIR surrounding the 1-to-1 line (black line). All uncertainties are 1σ based on measurement uncertainties (uncertainty from the VBD correction itself has not been propagated as the standard error for the estimate [0.14 wt%] is smaller than the measurement uncertainty). Data from [8, 25]: samples are experimental basaltic glasses based on compositions from Masaya (MAS) and Stromboli (St).

A comparison of calibrated-VBD using EPMA to other techniques often used to measure the H_2O content of melt inclusions, matrix glass, and experimental samples – such as Raman spectroscopy, transmission Fourier transform infrared (FTIR) spectroscopy, and secondary ion mass spectrometry (SIMS) – is shown for hydrous basaltic glass in Fig. 3 (see [7] for an overview of different techniques for measuring water in the context of melt inclusion analysis). The spatial resolution of EPMA (~5 µm diameter) is higher than transmission-FTIR and SIMS (~10 µm diameter, although higher spatial resolution is possible using synchrotron or focal-plane-array FTIR) but lower than Raman (~1 µm diameter). The analytical uncertainty for EPMA (±0.7 wt%) is larger than for Raman (±0.2 wt%), transmission-FTIR (approximately ±13%, equivalent of ±0.65 wt% at 5 wt% H_2O), and SIMS (approximately ±5%, equivalent of ±0.25 wt% at 5 wt% H_2O). Sample preparation for EPMA, Raman, and SIMS requires a single-polished surface, whereas transmission-FTIR requires doubly-polished surfaces (although a single-polished surface can be used in attenuated-total-reflectance FTIR). EPMA measures the major and minor element chemistry at the same time as VBD, whereas Raman can be used to measure sub-surface, unexposed

melt inclusions; FTIR can also measure CO_2 concentration and volatile speciation; and SIMS can also measure CO_2 concentration and isotope ratios. Hence, there are benefits and drawbacks to each technique but, as EPMA is often required regardless to measure the major and minor element chemistry, the addition of calibrating VBD to also get H_2O is very useful.

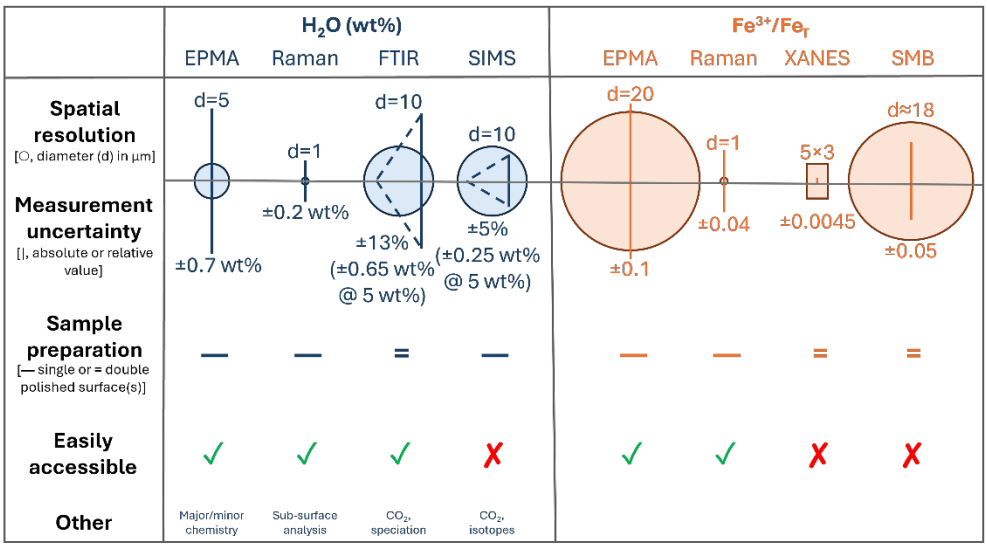

Fig. 3. Comparison between microanalytical techniques to measure H_2O (EPMA, Raman spectroscopy, transmission Fourier transform infrared spectroscopy = FTIR, and secondary ion mass spectrometry = SIMS) and Fe^{3+}/Fe_T (EPMA, Raman, X-ray absorption near-edge structure spectroscopy = XANES, synchrotron Mössbauer spectroscopy = SMB) for spatial resolution (area of circle/rectangle is proportional to analytical area, d = diameter in µm); measurement uncertainty (length of vertical line is proportional to absolute uncertainty: where % uncertainties are appropriate, the absolute uncertainty is shown from 0 to 5 wt% H_2O); sample preparation requirements; accessibility; and other considerations.

3 Iron oxidation state using the time-dependent-ratio flank method

The oxidation state of Fe can be quantified using EPMA by analysing the Fe$L\alpha$ and Fe$L\beta$ lines [26] or indirectly using stoichiometry [27]. Stoichiometry cannot be applied to silicate glass, hence we focus on the use of the FeL lines. The energy of X-ray emission (Fe$L\alpha$ and Fe$L\beta$) and absorption (L_3 and L_2 absorption edges) associated with the FeL lines are very similar leading to self-absorption [28]. The energy of the emission and absorption edges shift due to changes in the coordination and oxidation state of Fe, and the degree of self-absorption varies with the accelerating voltage and Fe concentration [26, 29-30]. Together, this means the peak positions and intensities of Fe$L\alpha$ and Fe$L\beta$ vary depending on Fe oxidation state, coordination, and concentration (Fig. 4A) and have been used to measure Fe^{3+}/Fe_T in a variety of geological minerals [e.g., 20-34] and glasses [9, 35-37]. The "peak shift" method correlates the wavelength position of Fe$L\alpha$ measured using wavescans with Fe^{3+}/Fe_T [35]. Alternatively, the "flank" method correlates the ratio of the intensities measured on the high-wavelength flank of Fe$L\beta$ (Fe$L\beta_f$) to the low-wavelength flank of Fe$L\alpha$ (Fe$L\alpha_f$) – termed the flank ratio – with Fe^{2+}, which is converted to Fe^{3+}/Fe_T using the known Fe content [30].

The FeL lines have weak intensities requiring high beam currents and/or long count times to achieve reasonable counting statistics. This is problematic when analysing silicate glass because they are beam sensitive due to sub-surface charging. As well as element migration, this causes reduction of Fe in anhydrous, high-Fe^{3+}/Fe_T glasses and oxidation of Fe in hydrous

and/or alkali-rich, low-Fe^{3+}/Fe_T glasses with the rate of oxidation/reduction depending on glass composition and analytical conditions [9, 35-36, 38]. To mitigate for this, the sample can be moved during analysis to minimize the beam damage in any particular area [36], but this decreases spatial resolution significantly (~240×10 μm^2). Alternatively, a TDI correction can be applied enabling much higher spatial resolution (20–60 μm diameter), which requires using the flank method as it is much easier to correct intensity measurements at two wavelengths using TDI than over a wavescan [9]. This is called the time-dependent-ratio (TDR) flank method [9].

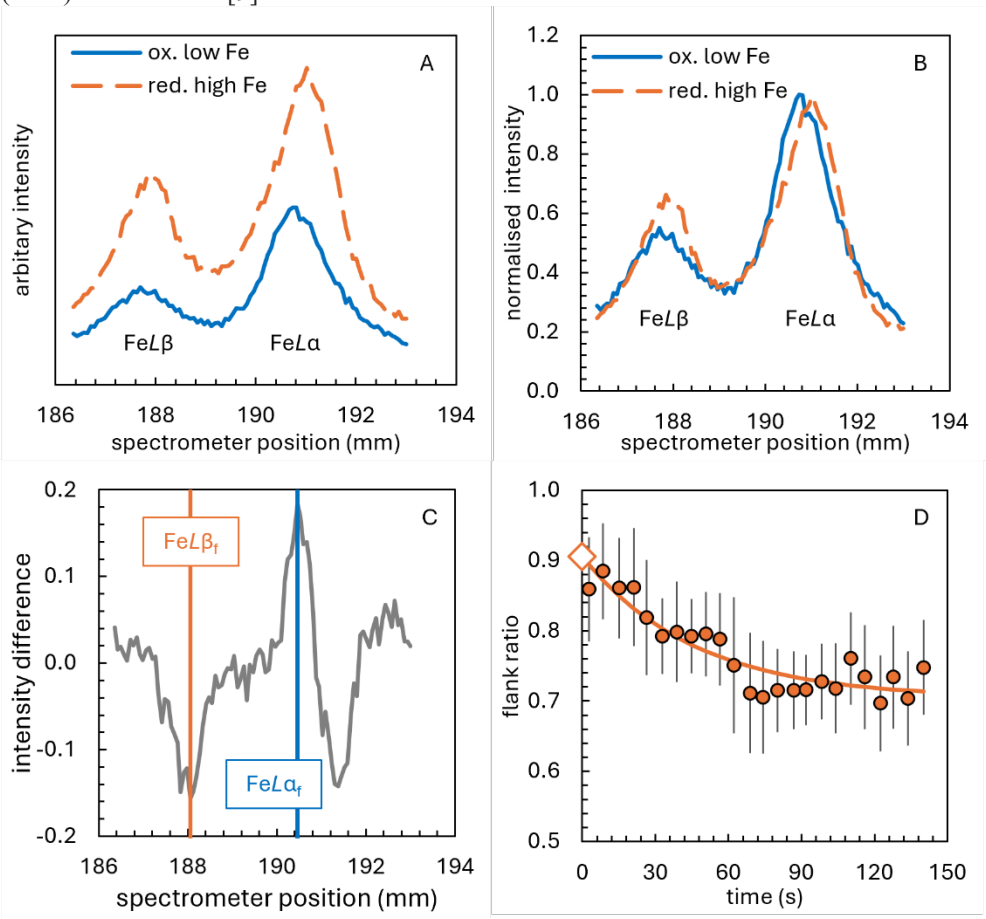

Fig. 4. (A) Fe*L* wavescans of an anhydrous basaltic glass that is oxidised (ox., i.e., high Fe^{3+}/Fe_T) and contains low Fe_T (solid) and an anhydrous tephriphonolitic glass that is reduced (red., i.e. low Fe^{3+}/Fe_T) and contains high Fe_T (dash). **(B)** Wavescans from (A) have been normalised to the intensity of their Fe*Lα* peak. **(C)** Difference spectrum between wavescans in (B) [oxidised-low-Fe – reduced-high-Fe], with flank positions (Fe$L\alpha_f$ and Fe$L\beta_f$) shown by vertical solid lines. **(D)** Flank ratio over time (filled circles, uncertainties are 1σ), where the open diamond is the initial flank ratio and the solid curve is the fit using eq. (1) for a hydrous basaltic glass. Data from [9]: all samples are experimental glasses.

Identifying flank positions is time consuming but if measured relative to an easy to measure peak (termed the flank reference peak; e.g., F*Kα* on MgF_2 or 2nd order Al*Kα* on Al_2O_3), only needs to be done once per instrument. An example EPMA set-up for identifying flank positions is shown in Table 2 [9]. Wavescans are collected on two glasses with Fe_T and Fe^{3+}/Fe_T that are as different as possible (i.e., high-Fe_T and low-Fe^{3+}/Fe_T vs. low-Fe_T and high-Fe^{3+}/Fe_T) with the stage moving (1 μ s^{-1}) to avoid beam damage (Fig. 4A). Multiple

wavescans are collected on each glass combining counts from all TAP-type crystals on the instrument to improve signal-to-noise. The difference spectrum is calculated by subtracting the wavescans normalized to the intensity of their Fe$L\alpha$ peak (Fig. 4B), where the flank positions are the minimum (Fe$L\beta_f$) and maximum (Fe$L\alpha_f$) in the difference spectrum (Fig. 4C).

Table 2. Example EPMA set-up for identifying flank positions from [9].

Analytical conditions		
Accelerating voltage (kV)	Beam current (nA)	Beam diameter (μm)
15	50	10
Wavescan set-up		
Number of steps	Step size (mm, JEOL only)	Dwell time (s)
100	0.071	0.5

Notes: Stage must be moving (1 μ s^{-1}) during analysis. Accelerating voltage must be the same as used for analysing unknowns.

An example EPMA set-up for using the TDR flank method is shown in Table 3 [9]. Counting statistics are maximised by using all TAP-type crystals available on the instrument to measure at flank positions, combining multiple crystals on Fe$L\alpha_f$ and/or Fe$L\beta_f$ to optimise the overall intensity measured (e.g., accounting for the count rate on the specific TAP-type crystal and that Fe$L\beta$ is less intense than the Fe$L\alpha$). Depending on how many and what spectrometers are left, sample homogeneity and beam damage can be monitored using Fe$K\alpha$ and K$K\alpha$. Initially, TAP-type crystals are peaked on the flank reference peak, which is used to set pulse height analysis (PHA) windows, where differential mode removes the 9th order Fe$K\alpha$. Peak positions are then set to the flank positions using the known offsets relative to the flank reference peak. Multiple TDI analyses (e.g., ten) are typically averaged for a single glass (i.e., melt inclusion or experimental glass) to achieve reasonable uncertainties on Fe^{3+}/Fe_T (±0.1). The beam diameter is selected to balance the sample area available whilst ensuring the rate of the flank ratio change is slow enough to be corrected using TDI. For instance, a 4 μm beam diameter is appropriate for basaltic glass (total area for 10 analyses ≈ 20 μm diameter), whereas 15 μm is required for peralkaline rhyolitic glass (total area for ten analyses ≈ 60 μm diameter). The largest beam diameter that can be used is ~20 μm, above which the spectrometers can defocus.

Table 3. Example EPMA set-up for TDR flank measurements from [9].

Analytical conditions		
Accelerating voltage (kV)	Beam current (nA)	Beam diameter (μm)
15	50	4–15*
Count times		
Number of intervals	Interval time (s)	Total time (s)
24	5	~150

Notes: As many TAP-type crystals as available are used to measure the flank positions. *Depends on beam damage sensitivity.

There are multiple options for data processing. One option is to calculate the flank ratio with time from the measured intensities on Fe$L\alpha_f$ and Fe$L\beta_f$ and then calculate the initial flank ratio (I_0) by fitting either an exponential function (solving for I_0, I_∞, and $\dot{I}_0$):

$$I_t = (I_0 - I_\infty)e^{\left(\frac{\dot{I}_0 t}{I_0 - I_\infty}\right)} + I_\infty \quad (1)$$

where I is the flank ratio and the subscript refers to time t; a straight line ($I_t = \dot{I} \cdot t + I_0$); or taking the average if the flank ratio is constant over time (Fig. 4D; e.g., *R*-code from [9]). Alternatively, the data can be collected and processed within the *Probe for EPMA* software, which applies a TDI-correction to each measured intensity, from which the initial ratio can be calculated. There is also the open-source *Flank Reduction* tool through a web-application with a graphical user interface [39], which has been applied to garnets. The Fe^{2+} of the unknown glasses is calculated using a calibration curve of I_0 against Fe^{2+} constructed using standards of known Fe^{3+}/Fe_T. To convert Fe^{2+} to Fe^{3+}/Fe_T, the Fe concentration measured using standard EPMA is used (e.g., using set-up in Table 1: standard EPMA should be done before TDR flank measurements to avoid beam damage). An example application is shown in Figure 5, where the oxygen fugacity is calculated from the measured Fe^{3+}/Fe_T of hydrous basaltic glasses using the TDR flank method, showing these experiments ranged from ΔNNO-1 to +4 [40].

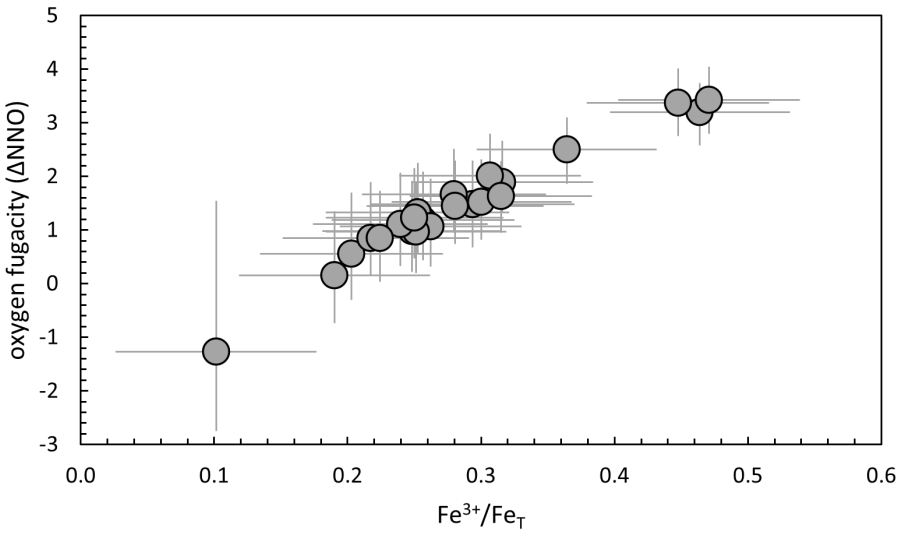

Fig. 5. An example application of the TDR flank method to hydrous, basaltic, experimental glasses showing the calculated oxygen fugacity (ΔNNO, which is relative to the nickel-nickel oxide buffer) from the TDR flank method Fe^{3+}/Fe_T. Data from [40].

A comparison of the TDR-flank method using EPMA to other techniques often used to measure Fe^{3+}/Fe_T in silicate glass – such as Raman, X-ray absorption near-edge structure (XANES) spectroscopy, and synchrotron Mössbauer (SMB) spectroscopy – is shown for hydrous basaltic glass in Fig. 3 (see [41] for an overview of different techniques for measuring the oxidation state of Fe and other elements in geological materials). EPMA (~20 μm diameter) has a similar spatial resolution to SMB (~18 μm diameter), which are much lower than XANES (5 × 3 μm^2) or Raman (~1 μm diameter). The absolute uncertainty for EPMA (±0.1) is double SMB (±0.05) and Raman (±0.04) and over an order of magnitude larger than XANES (±0.0045). Sample preparation and accessibility are much simpler for EPMA and Raman, requiring a single-polished surface and often available in-house; whereas XANES and SMB require doubly-polished surfaces and access to a synchrotron.

4 Conclusion

We have outlined two electron probe techniques that enable the water content and Fe^{3+}/Fe_T to be quantified in hydrous silicate glass – in addition to the major and minor element composition typically analysed by EPMA – and compare them to other techniques available for such analyses. These EPMA techniques mitigate the effects of sub-surfacing charging that causes element migration, iron oxidation and reduction, and reduced X-ray emission through calibration and TDI corrections, improving accuracy and precision. The high spatial resolution of EPMA means these techniques can be applied to small sample areas – such as melt inclusions, matrix glass, and experimental glasses – to study magmatic and volcanic processes.

Hughes gratefully acknowledges the Bastin PhD Thesis Award (2025) from the European Microbeam Analysis Society (EMAS) and Thermo Fisher Scientific. A special thank you goes to Heidy Mader, who passed away in 2022, for all her help and support of this work during Hughes's PhD thesis. We thank Alejandro Cortes and Francesca Piccoli for their helpful reviews that improved the manuscript and Bjørn Eske Sørensen for his editorial handling of the manuscript. This paper has been adapted from [42]. ECH was supported by a NERC GW4+ DTP studentship from the Natural Environment Research Council (NE/L002434/1) and additional funding and support from CASE partner Te Pū Ao GNS Science (now Earth Sciences New Zealand). ECH and GK were supported by the New Zealand Ministry of Business, Innovation and Employment (MBIE) through the Hazards and Risk Management Programme (Strategic Science Investment Fund, contract CO5X1702). All data is available in [8-10, 40]. ECH wrote the original draft of the paper and all authors contributed to the original work described in the paper, as well as reviewing and editing the paper.

References

1. M. Edmonds, P.J. Wallace, Volatiles and exsolved vapor in volcanic systems. Elements. **13**, 29–34 (2017). https://doi.org/10.2113/gselements.13.1.29
2. D.L. Hamilton, C.W. Burnham, E.F. Osborn, The solubility of water and effects of oxygen fugacity and water content on crystallization in mafic magmas. J. Petrol. **5**, 21-39 (1964). https://doi.org/10.1093/petrology/5.1.21
3. D.B. Dingwell, D. Virgo, The effect of oxidation state on the viscosity of melts in the system Na_2O-FeO-Fe_2O_3-SiO_2. Geochim. Cosmochim. Acta **51**, 195-205 (1987). https://doi.org/10.1016/0016-7037(87)90231-6
4. E.C. Hughes, P. Liggins, L. Saper, E.M. Stolper, The effects of oxygen fugacity and sulfur on the pressure of vapor-saturation of magma. Am. Min. 2024 **109**, 422-438 (2024). https://doi.org/10.2138/am-2023-8739
5. D. Giordano, D. Dingwell, Viscosity of hydrous Etna basalt: Implications for Plinian style basaltic eruptions. Bull. Volcanol. **65**, 8-14 (2003). https://doi.org/10.1007/s00445-002-0233-2
6. S.T. Feig, J. Koepke, J.E. Snow, Effect of water on tholeiitic basalt phase equilibria: An experimental study under oxidizing conditions. Contrib. Mineral. Petrol. **152**, 611-638 (2006). https://doi.org/10.1007/s00410-006-0123-2
7. E.F. Rose-Koga, A.-S. Bouvier, G.A. Gaetani, P.J. Wallace, C.M. Allison, J.A. Andrys, C.A. Angeles de la Torre, A. Barth, R.J. Bodnar, A.J.J. Bracco Gartner, D. Butters, A. Castillejo, B. Chilson-Parks, B.R. Choudhary, N. Cluzel, M. Cole, E. Cottrell, A. Daly, L.V. Danyushevsky, C.L. DeVitre, M.J. Drignon, L. France, M. Gaborieau, M.O. Garcia, E. Gatti, F.S. Genske, M.E. Hartley, E.C. Hughes, A.A. Iveson, E.R. Johnson, M. Jones, T. Kagoshima, Y. Katzir, M. Kawaguchi, T. Kawamoto, K.A. Kelley, J.M. Koornneef, M.D. Kurz, M. Laubier, G.D. Layne, A.

Lerner, K.-Y. Lin, P.-P. Liu, A. Lorenzo-Merino, N. Luciani, N. Magalhães, H.R. Marschall, P.J. Michael, B.D. Monteleone, L.R. Moore, Y. Moussallam, M. Muth, M.L. Myers, D.F. Narváez, O. Navon, M.E. Newcombe, A.R.L. Nichols, R.L. Nielsen, A. Pamukcu, T. Plank, D.J. Rasmussen, J. Roberge, F. Schiavi, D. Schwartz, K. Shimizu, K. Shimizu, N. Shimizu, J.B. Thomas, G.T. Thompson, J.M. Tucker, G. Ustunisik, C. Waelkens, Y. Zhang, T. Zhou, Silicate melt inclusions in the new millennium: A review of recommended practices for preparation, analysis, and data presentation. Chem. Geol. **570**, 120145 (2021). https://doi.org/10.1016/j.chemgeo.2021.120145

8. E.C. Hughes, B. Buse, S.L. Kearns, J.D. Blundy, G. Kilgour, H.M. Mader, Low analytical totals in EPMA of hydrous silicate glass due to sub-surface charging: Obtaining accurate volatiles by difference. Chem. Geol. **505**, 48-56 (2019). https://doi.org/10.1016/j.chemgeo.2018.11.015
9. E.C. Hughes, B. Buse, S.L. Kearns, J.D. Blundy, G. Kilgour, H.M. Mader, R.A. Brooker, R. Balzer, R.E. Botcharnikov, D. Di Genova, R.R. Almeev, J.M. Riker, High spatial resolution analysis of the iron oxidation state in silicate glasses using the electron probe. Am. Min. **103**, 1473-1486 (2018). https://doi.org/10.2138/am-2018-6546CCBY
10. E.C. Hughes, P. Liggins, P. Wieser, E.M. Stolper, VolFe: an open-source Python package for calculating melt-vapor equilibria including silicate melt, carbon, hydrogen, sulfur, and noble gases. Earth ArXiv (pre-print). https://doi.org/10.31223/X52X3G
11. J.D. Blundy, K.V. Cashman, Petrologic reconstruction of magmatic system variables and processes. Rev. Mineral. Geochem. **69**, 179–239 (2008). https://doi.org/10.2138/rmg.2008.69.6
12. J.D. Devine, J.E. Gardner, H.P. Brack, G.D. Laynet, M.J. Rutherford, Comparison of microanalytical methods for estimating H_2O contents of silicic volcanic glasses. Am. Min. **80**, 319–328 (1995). https://doi.org/10.2138/am-1995-3-413
13. M.C.S. Humphreys, S.L. Kearns, J.D. Blundy, SIMS investigation of electron-beam damage to hydrous, rhyolitic glasses: Implications for melt inclusion analysis. Am. Min. **91**, 667-679 (2006). https://doi.org/10.2138/am.2006.1936
14. P.L. King, T.W. Vennemann, J.R. Holloway, R.L. Hervig, J.B. Lowenstern, J.F. Forneris, Analytical techniques for volatiles: A case study using intermediate (andesitic) glasses. Am. Min. **87**, 1077-1089 (2002). https://doi.org/10.2138/am-2002-8-904
15. W.P. Nash, Analysis of oxygen with electron microprobe: Applications to hydrated glass and minerals. Am. Min. **77**, 453-457 (1992).
16. J.J. Donovan, E.P. Vicenzi, Water by EPMA- New developments. Microsc. Microanal. **14**, 1274-1275 (2008). https://doi.org/10.1017/S1431927608082615
17. D.C. Roman, K.V. Cashman, C.A. Gardner, P.J. Wallace, J.J. Donovan, Storage and interaction of compositionally heterogeneous magmas from the 1986 eruption of Augustine Volcano, Alaska. Bull. Volcanol. **68**, 240-254 (2006). https://doi.org/10.1007/s00445-005-0003-z
18. J.J. Donovan, T.N. Tingle, An improved mean atomic number background correction for quantitative microanalysis. Microsc. Microanal. **2**, 1-7 (1996). https://doi.org/10.1017/S1431927696210013
19. M.R. Carroll, M.J. Rutherford, Sulfur speciation in hydrous experimental glasses of varying oxidation state: Results from measured wavelength shifts of sulfur X-rays. Am. Min. **73**, 845-849 (1998).

20. J. Cazaux, Electron probe microanalysis of insulating materials: Quantification problems and some possible solutions. X-Ray Spectrom. **25**, 265-280 (1996). https://doi.org/10.1002/(SICI)1097-4539(199611)25:6<265::AID-XRS172>3.0.CO;2-3
21. C.H. Nielsen, H. Sigurdsson, Quantitative methods for electron microprobe analysis of sodium in natural and synthetic glasses. Am. Mineral. **66**, 547-552 (1981).
22. G.B. Morgan, D. London, 2005. Effect of current density on the electron microprobe analysis of alkali aluminosilicate glasses. Am. Min. **90**, 1131-1138 (2005). https://doi.org/10.2138/am.2005.1769
23. C. Bonnelle, Charge trapping in dielectrics. Microsc. Microanal. **10**, 691-696 (2004). https://doi.org/10.1017/S1431927604040620
24. E. Médard, T.L. Grove, The effect of H_2O on the olivine liquidus of basaltic melts: Experiments and thermodynamic models. Contrib. Mineral. Petrol. **155**, 417-432 (2008). https://doi.org/10.1007/s00410-007-0250-4
25. P. Lesne, S.C. Kohn, J.D. Blundy, F. Witham, R.E. Botcharnikov, H. Behrens, Experimental simulation of closed-system degassing in the system basalt-H_2O-CO_2-S-Cl. J. Petrol. **52**, 1737-1762 (2011). https://doi.org10.1093/petrology/egr027
26. P. Gopon, J. Fournelle, P.E. Sobol, X. Llovet, Low-voltage electron probe microanalysis of Fe–Si compounds using soft X-rays. Microsc. Microanal. **19**, 1698-1708 (2013). https://doi.org/10.1017/S1431927613012695
27. D.A. Neave, A.G. Stewart, M.E. Hartley, C. McCammon, Re-evaluating stoichiometric estimates of iron valence in magmatic clinopyroxene crystals. Contrib. Mineral. Petrol. **179**, 5 (2024). https://doi.org/10.1007/s00410-023-02080-2
28. D.G.W. Smith, R.K. O'Nions, Investigations of the $L_{II, III}$ X-ray emission spectra of Fe by the electron microprobe Part I: Some aspects of the Fe $L_{II, III}$ spectra from metallic iron and haematite. J. Phys. D: Appl. Phys., **4**, 147-159 (1971). https://doi.org/10.1088/0022-3727/4/1/320
29. F. de Groot, High-resolution X-ray emission and X-ray absorption spectroscopy. Chem. Rev. **101**, 1779-1808 (2001). https://doi.org/10.1021/cr9900681
30. H.E. Höfer, G.P. Brey, The iron oxidation state of garnet by electron microprobe: Its determination with the flank method combined with major element analysis. Am. Min. **92**, 873-885 (2007). https://doi.org/10.2138/am.2007.2390
31. M. Enders, D. Speer, W.V. Maresch, C.A. McCammon, Ferric/ferrous iron ratios in sodic amphiboles: Mössbauer analysis, stoichiometry-based model calculations and the high-resolution microanalytical flank method. Contrib. Mineral. Petrol. **140**, 135-147 (2000). https://doi.org/10.1007/s004100000179
32. M. Holycross, E. Cottrell, J. Ague, A. Lanzirotti, M. Newville, Fe Kα XANES, Fe Kβ HERFD XANES and EPMA flank method determinations of the oxidation state of Fe in garnet. Chem. Geol. **647**, 121937 (2024). https://doi.org/10.1016/j.chemgeo.2024.121937
33. Y. Cao, C.-M. Xing, C.Y. Wang, X. Ping, Determination of the oxidation state of iron in calcic pyroxene using the electron microprobe flank method. Am. Min. (2025). https://doi.org/10.2138/am-2024-9467
34. X. Li, C. Zhang, R.R. Almeev, X.-C. Zhang, X.-F. Zhao, L.-X. Wang, J. Koepke, F. Holtz, Electron probe microanalysis of $Fe^{2+}/\Sigma Fe$ ratios in calcic and sodic-calcic amphibole and biotite using the flank method. Chem. Geol. **509**, 152-162 (2019). https://doi.org/10.1016/j.chemgeo.2019.01.009

35. M. Fialin, A. Bézos, C. Wagner, E. Humler, (2004) Quantitative electron microprobe analysis of $Fe^{3+}/\Sigma Fe$: Basic concepts and experimental protocol for glasses. Am. Min. **89**, 654-662 (2004). https://doi.org/10.2138/am-2004-0421
36. C. Zhang, R.R. Almeev, E.C. Hughes, A. Borisov, E. Wolff, H.E. Höfer, R.E. Botcharnikov, J. Koepke, J. (2018) Electron microprobe technique for the determination of iron oxidation state in silicate glasses. Am. Min. **103**, 1445-1454 (2018). https://doi.org/10.2138/am-2018-6437
37. J. Marcial, J. George, P. Ferkl, R. Pokorný, R. Kissinger, C.I. Pearce, J.V. Crum, J. Klouzek, P. Hrma, A.A. Kruger, Elemental mapping and iron oxidation state measurement of synthetic low-activity waste feeds. J. Non-Cryst. Solids **591**, 121725 (2022). https://doi.org/10.1016/j.jnoncrysol.2022.121725
38. E.C. Hughes, B. Buse, S.L. Kearns, R.A. Brooker, D. Di Genova, G. Kilgour, H.M. Mader, J.D. Blundy, The microanalysis of iron and sulphur oxidation states in silicate glass - Understanding the effects of beam damage. IOP Conf. Ser.: Mater. Sci. Eng. **891**, 012014. https://doi.org/10.1088/1757-899X/891/1/012014
39. D.C. Hezel, H.E. Höfer, A. Fichtner, A fast open data reduction workflow for the electron microprobe flank method to determine $Fe^{3+}/\Sigma Fe$ contents in minerals. Am. Min. **109**, 1387-1393 (2024). https://doi.org/10.2138/am-2023-9122
40. E. C. Hughes, Microanalytical techniques and experimental studies of the volatile and fO2 history of magmas using melt inclusions, Ph.D. thesis, University of Bristol, School of Earth Sciences (2019)
41. D.R. Neuville, M.R. Cicconi, C. Le Losq, How to measure the oxidation state of multivalent elements in minerals, glasses, and melts? In R. Moretti & D.R. Neuville (Eds.), Magma Redox Geochemistry (2021). https://doi.org/10.1002/9781119473206.ch13
42. E.C. Hughes, B. Buse, S.L. Kearns, G. Kilgour, H. Mader, J. Blundy, Analysing silicate melt inclusions, in Book of Tutorials and Abstracts, EMAS 2018: 13th Regional Workshop on "Microbeam Analysis in the Earth Sciences", University of Bristol, Great Britain, September 4-7 (2018).